ARTICLE Open Access

Room-temperature waveguide-integrated photodetector using bolometric effect for mid-infrared spectroscopy applications

Joonsup Shim[1], Jinha Lim[1], Inki Kim[1], Jaeyong Jeong[1], Bong Ho Kim[1], Seong Kwang Kim[1], Dae-Myeong Geum[2] and SangHyeon Kim[1]✉

Abstract

Waveguide-integrated mid-infrared (MIR) photodetectors are pivotal components for the development of molecular spectroscopy applications, leveraging mature photonic integrated circuit (PIC) technologies. Despite various strategies, critical challenges still remain in achieving broadband photoresponse, cooling-free operation, and large-scale complementary-metal-oxide-semiconductor (CMOS)-compatible manufacturability. To leap beyond these limitations, the bolometric effect – a thermal detection mechanism – is introduced into the waveguide platform. More importantly, we pursue a free-carrier absorption (FCA) process in germanium (Ge) to create an efficient light-absorbing medium, providing a pragmatic solution for full coverage of the MIR spectrum without incorporating exotic materials into CMOS. Here, we present an uncooled waveguide-integrated photodetector based on a Ge-on-insulator (Ge-OI) PIC architecture, which exploits the bolometric effect combined with FCA. Notably, our device exhibits a broadband responsivity of 28.35%/mW across 4030–4360 nm (and potentially beyond), challenging the state of the art, while achieving a noise-equivalent power of 4.03×10^{-7} W/Hz$^{0.5}$ at 4180 nm. We further demonstrate label-free sensing of gaseous carbon dioxide (CO_2) using our integrated photodetector and sensing waveguide on a single chip. This approach to room-temperature waveguide-integrated MIR photodetection, harnessing bolometry with FCA in Ge, not only facilitates the realization of fully integrated lab-on-a-chip systems with wavelength flexibility but also provides a blueprint for MIR PICs with CMOS-foundry-compatibility.

Introduction

The mid-infrared (MIR) spectral region beyond 3 μm is of enormous scientific and technological importance, as it encompasses unique molecular fingerprints[1–3], enabling sophisticated chemical and biological analysis in a non-invasive manner through absorption spectroscopy techniques[4,5]. Leveraging highly mature photonic integrated circuit (PIC) technologies[6–8], substantial progress has been made in miniaturizing traditional external-optics-based spectrometers into chip-scale systems that offer cost-effective, mass-manufacturable, and scalable solutions[9–12]. A key bottleneck in realizing fully integrated and robust lab-on-a-chip systems is the monolithic integration of MIR photodetectors (PDs) into the waveguide platforms, which are an indispensable building block of PICs to convert light into electrical signals. Traditionally, surface-illuminated MIR PDs have relied on narrow-bandgap semiconductor materials such as HgCdTe alloy[13] and III-V compounds[14]; yet, they necessitate cryogenic cooling (bulky and costly) to mitigate high thermal noise at room temperature, posing severe challenges in practical applications[15]. More recently, two-dimensional materials (e.g., graphene[16] and black phosphorus[17]) have arisen as promising candidates that can be operated at room temperature[18]. However, the zero-bandgap nature of graphene results in an extremely high dark current level

Correspondence: SangHyeon Kim (shkim.ee@kaist.ac.kr)
[1]School of Electrical Engineering, Korea Advanced Institute of Science and Technology (KAIST), 291 Daehak-Ro, Yuseong-Gu, Daejeon 34141, Republic of Korea
[2]Department of Electrical & Computer Engineering, Inha University, 100, Inha-ro, Michuhol-gu, Incheon 22212, Republic of Korea

under biasing[19]. Additionally, black phosphorus itself exhibits severe performance degradation under ambient conditions and possesses an absorption edge of around 4 μm[20], restricting its utility to longer wavelengths. These emerging materials also still struggle with complementary-metal-oxide-semiconductor (CMOS)-compatible processes and wafer-scale integration, impeding large-scale and cost-saving production at commercialization levels[21].

In this regard, it is highly beneficial for MIR photodetection to harness thermal-type PDs, where the photoresponse is extracted by converting photo-induced heat generation into the electrical signal[18,22,23], enabling wavelength-insensitive photodetection by properly tailoring the spectral characteristics of the light absorber. Owing to the inherent nature of thermal detection, there is a slight compromise in response speed; however, a relatively moderate (or even low) level of bandwidth is adequate to meet the requirements for many MIR spectroscopy applications. To reap the full benefits of superior properties of the thermal detectors including wavelength independence and uncooled photodetection, here, we introduce the bolometric effect into the waveguide platform. Bolometers, a class of thermal-type PD, convert light-induced temperature fluctuations into changes in electrical resistance[23–25]. Notably, to date, few efforts have been devoted to achieving waveguide-integrated MIR photodetection beyond 3 μm using thermal detection mechanisms[26–29]. Optical absorbers with gold (Au) antennas on a suspended-Si waveguide have shown promise in bolometry in the range of 3.72–3.88 μm[26,27]; however, they offer low responsivities, and the resonance nature of the plasmonic structure intrinsically limits broadband photodetection. Additionally, the usage of noble metals is commonly restricted in CMOS foundries. Graphene-based detectors using the photothermoelectric (PTE) effect, another class of thermal detection mechanism based on the temperature-gradient-driven voltage generation governed by the Seebeck coefficient of the thermoelectric materials[30], have shown promising results on waveguide platforms such as chalcogenide glass (ChG)-on-CaF_2 at 5.2 μm[28] and Ge-on-Si (GOS) at 3.7 μm[29]. These graphene-based PTE detectors are particularly attractive due to their zero-bias operation and fast response times. However, their usage is limited to a wavelength range of ~8 μm due to the inherent material properties of the photonic platform, which restrict their utility across the broader MIR band. In addition, the use of plasmonic Au strips[29] and a split-gate architectures[28,29] introduces further fabrication challenges, including misalignment and errors during transfer and patterning of graphene. A more comprehensive comparison between bolometric and PTE detectors is provided in the *Discussion* section.

In this work, we remarkably advance the state of the art in waveguide-integrated MIR PDs by exploiting the bolometric effect with free-carrier absorption (FCA) in Ge[31,32] and titanium oxide-based bolometric material[33–35], providing a pragmatic approach with high fabrication robustness for uncooled MIR photodetection without foreign materials in CMOS or hybrid integrations. Our demonstration is based upon a CMOS-compatible Ge-on-insulator (Ge-OI) photonic platform with a buried oxide (BOX) of Y_2O_3 and a Si substrate, providing broad transparency window up to around 13 μm[36–40], and reaches record-high photoresponsivity for waveguide-integrated PDs using bolometric effect beyond 3 μm. Furthermore, to demonstrate the feasibility of non-destructive, label-free detection of molecules using our room-temperature-operated waveguide-integrated MIR PD, we have experimentally conducted gaseous carbon dioxide (CO_2) sensing by integrating the sensing waveguide and detector on a single chip.

Results

Device architecture and design

Figure 1a illustrates a schematic of the proposed MIR PIC-based sensor on the Ge-OI platform, comprising a slot waveguide for analyte sensing (passive sensing part) and a waveguide-integrated PD (detector part), monolithically integrated onto a single chip. Our on-chip photonic sensor utilizes light–analyte interaction within the sensing waveguide through absorption spectroscopy[38,40] based on the Beer-Lambert law. An air-clad slot waveguide, supporting hollow-core guiding, has been employed to induce stronger light absorption with enhanced field confinement compared to conventional strip or rib waveguides, thus aiming to improve the sensitivity factor or to reduce the physical length of the sensing waveguide[11,36,38]. The residual light is then directly coupled from the sensing waveguide into the waveguide-integrated PD. As noted earlier, the operational principle of our proposed detector is the bolometric effect combined with FCA in Ge. For the bolometric material that converts light-induced temperature variations into changes in electrical resistance, we employed a TiO_2/Ti/TiO_2 tri-layer film, whose temperature-dependent electrical properties can be finely tailored by engineering the thickness of each layer[33–35]. The temperature change in bolometric detectors, in response to periodically varying incident light, can be described by[23]

$$\Delta T = \frac{\eta \Phi_0}{\sqrt{G_{th}^2 + \omega^2 \cdot C_{th}^2}} \quad (1)$$

where ΔT represents the temperature change, η is the absorption efficiency for the given wavelength, ω and Φ_0 are the angular frequency and the amplitude of the

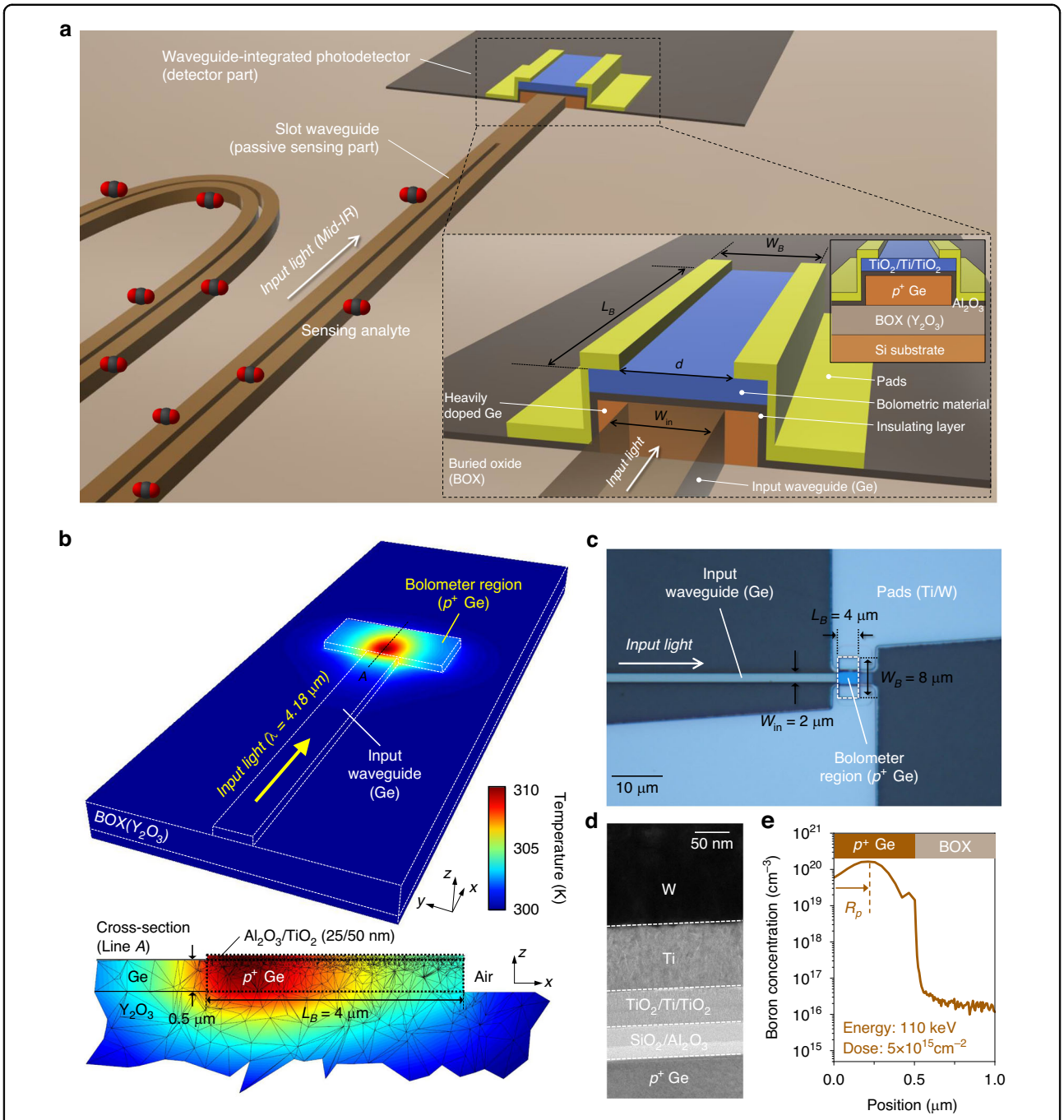

Fig. 1 Structure of the proposed device. a Illustration of the MIR PIC-based sensor on the Ge-OI platform consisting of the sensing waveguide and photodetector. The zoom-in view shows the schematic of the proposed waveguide-integrated photodetector using the bolometric effect combined with FCA in Ge. **b** Heat simulation (Ansys Lumerical) results showing steady-state temperature distribution within the proposed photodetector ($W_B = 8$ μm, $L_B = 4$ μm) for an incoming light at 4.18 μm (1 mW). Doping concentration of p^+ Ge region was assumed as 10^{20} cm^{-3}. Background temperature was set to be 300 K. **c** Optical microscope image of the fabricated device. **d** Cross-sectional TEM image of the device including the electrode region. **e** SIMS depth profile analysis indicating the boron-doped p^+ Ge region. The implant energy and dopant dose were 110 keV and 5×10^{15} cm^{-2}, respectively

periodic radiation, respectively, G_{th} is the thermal conductance between the detector and the surrounding environment, and C_{th} is the thermal capacitance of the detector. As inferred from Eq. (1), increasing η, while diminishing G_{th} and C_{th}, is critical for enhancing ΔT for a given incident optical power, which directly correlates

with the bolometric detector's responsivity. In order to boost η within our PD, FCA in Ge should be elevated, which greatly depends on the type of free carriers and the doping concentration for particular wavelengths. To take full advantage of FCA in Ge, we selected heavily-doped *p*-type Ge (p^+ Ge) as the MIR-absorbing medium (details can be found in Supplementary Note 1). For the reduction of G_{th} and C_{th}, optimizing device geometries is crucial. Here, the optimization process, including the geometrical parameters of the bolometer region – specifically, a length (L_B) of 4 μm and a width (W_B) of 8 μm – was conducted by considering heating efficiency, back-reflection, and in-house fabrication capabilities. The systematic process of optimizing geometries with numerical simulations is detailed in Supplementary Note 3. Figure 1b shows the simulated steady-state temperature distribution for the device designed with the final parameters. The input waveguide, having a width (W_{in}) of 2 μm, was designed to support only the fundamental transverse-electric (TE) mode. The incoming light was set to an optical power of 1 mW at a wavelength (λ) of 4.18 μm. As depicted in Fig. 1b, there is a significant temperature rise confined within the bolometer region. This localized heat generation is achieved by FCA within the p^+ Ge, which demonstrates the viability of an FCA-based thermalization process acting as a compact and efficient MIR absorber, even in the absence of resonance structures.

Figure 1c, d show the optical microscope and cross-sectional transmission electron microscopy (TEM) images, respectively, of the fabricated device on the Ge-OI photonic platform featuring a 500 nm-thick top Ge, a 2 μm-thick Y_2O_3 BOX, and a Si substrate. Here, the proposed waveguide-integrated PD incorporates a boron-doped p^+ Ge (bolometer region), a SiO_2/Al_2O_3 (20/25 nm) insulating layer stack, a bolometric material of $TiO_2/Ti/TiO_2$ (25/2/25 nm) tri-layer film, and a Ti/W (100/150 nm) metal electrode. The thickness of each layer in the bolometric material was carefully optimized (discussed in Supplementary Fig. S7). Additional characterizations, such as X-ray photoelectron spectroscopy (XPS) and X-ray diffraction (XRD), are detailed in Supplementary Figs. S9 and S10, respectively. Energy-dispersive X-ray spectroscopy (EDS) elemental mapping (see Supplementary Fig. S11) confirms the successful deposition of each layer. Secondary-ion mass spectrometry (SIMS) depth profile analysis in Fig. 1e quantitatively reveals the impurity dopant concentration within the p^+ Ge region. To make full use of FCA in Ge, ion implantation was performed with a high dopant dose of $5 \times 10^{15}\,cm^{-2}$, and the implant energy was carefully adjusted to 110 keV. This optimization contributes to exposing a larger fraction of the modal field to the peak doping-concentration region of the absorbing medium, aligning with the mode-field maximum and the projected range (R_p) of the implanted ions in the p^+ Ge.

Thermo-electrical characterization

We first investigated the temperature-dependent electrical properties. Figure 2a shows the current-voltage (*I-V*) curves from a voltage sweep ranging from −3.0 V to +3.0 V, with a 0.01-V interval, measured from 293 K to 363 K (1-K step), limited by our Peltier-driven stage. A nearly-linear characteristics with Ohmic behavior between the bolometric material and the electrode stack was obviously observed. Figure 2b plots the temperature-dependent current values at 3-V derived from the *I-V* curves, demonstrating a significant relationship with the temperature. Figure 2c presents the resistance-temperature (*R-T*) characteristics under constant-voltage mode, which can be modeled following equation to estimate the activation energy (ΔE):

$$R(T) = R_o \exp\left(\frac{\Delta E}{k_B T}\right) \tag{2}$$

where $R(T)$ denotes the temperature-dependent electrical resistance, T is the absolute temperature, R_o is a constant, and k_B is the Boltzmann constant. From Eq. (2), ΔE is extracted from the slope of the Arrhenius plot (ln(*R*) vs. 1000/T) shown in Fig. 2d, which was determined to be 0.315 eV within the measured temperature range. The temperature-dependent current modeling over a high-temperature range, based on the Arrhenius relationship by Eq. (2), is described in the inset of Fig. 2b, revealing a rapid, exponential increase in electrical current with rising temperature. However, beyond the certain threshold temperature range (~403 K), our device undergoes degradation due to oxidation-induced alterations in the structural properties of the bolometric material (as detailed in Supplementary Note 6).

To quantify the temperature dependence of the electrical resistance, temperature-coefficient of resistance (TCR), a crucial performance indicator for bolometric detectors, is introduced, which is defined as the derivative of resistance with respect to temperature,

$$\mathrm{TCR} = \left(\frac{1}{R}\right)\left(\frac{dR}{dT}\right) = -\frac{\Delta E}{k_B T^2} \tag{3}$$

Figure 2e shows the temperature-dependent TCR, as obtained by Eq. (3). Here, our device achieved a TCR of −4.262%/K at 293 K, the highest to date for waveguide-integrated PDs utilizing the bolometric effect, thus enhancing bolometric photodetection capabilities.

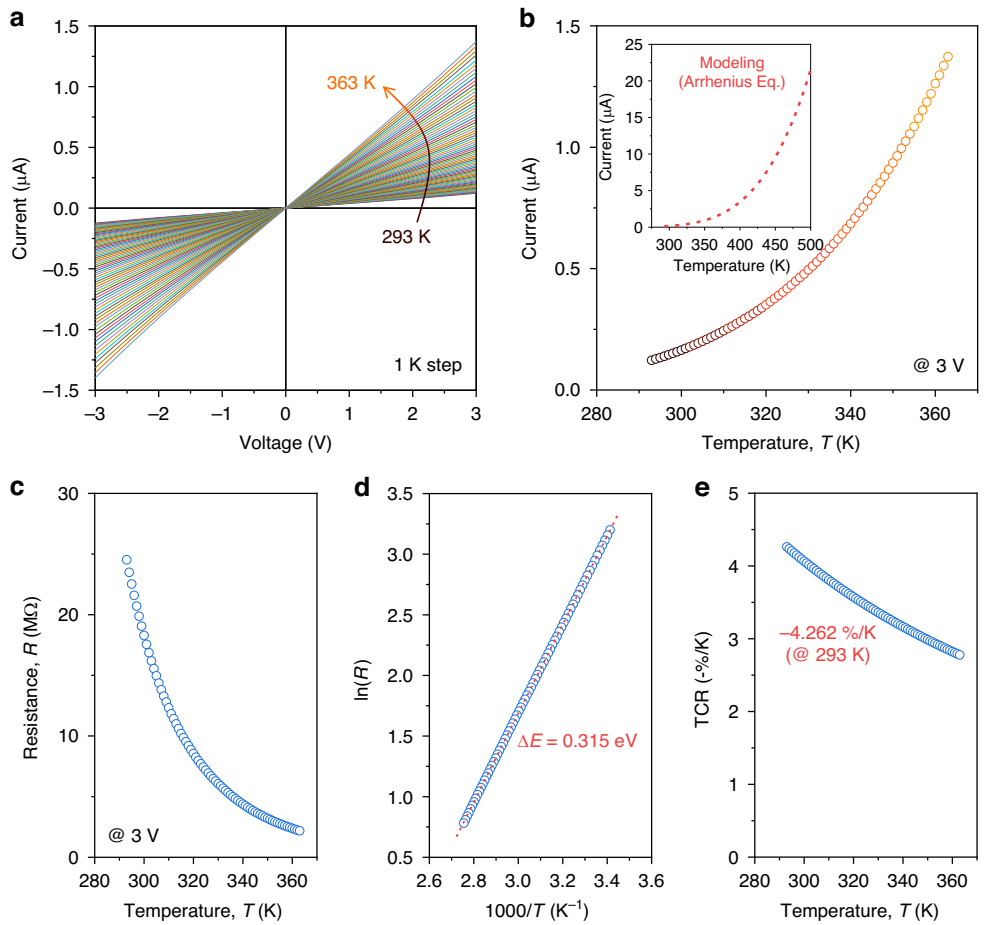

Fig. 2 Thermo-electrical characteristics. a Current-voltage (*I-V*) curves measured from 293 K to 363 K (1 K step), controlled by a Peltier-driven stage with a 10-mV interval. **b** Temperature dependence of current values at a 3-V biasing. The inset indicates the modeled current values depending on the temperature, calculated from the Arrhenius equation. **c** Resistance-temperature (*R-T*) characteristics under a 3-V biasing, following the Arrhenius relationship. **d** Arrhenius plot [ln(*R*) vs. 1000/*T*] with the activation energy (Δ*E*) calculated from the slope of the linear fit (red dashed line), indicating $\Delta E = 0.315$ eV. **e** TCR (-%/K) values depending on the temperature, showing −4.262%/K at 293 K

Photoresponse measurement

We now turn to explore the MIR photoresponse. The incident optical power coupled into the bolometer region was precisely calibrated, accounting for insertion losses from passive components with the assistance of an identical reference waveguide pattern without the detector part. A total insertion loss of 10.83 ± 0.14 dB (4.18 μm) was used for the calibration (details are provided in Supplementary Fig. S8). The un-illuminated *I-V* curve (off-state), plotted in the inset of Fig. 3a, reveals an off-state current (I_{off}) of 127.5 nA at a 3-V bias. Figure 3a presents the change in current, calculated as the ratio of the total measured current ($I_{ph} + I_{off}$) to I_{off}, as a function of optical power (P_{in}) and the corresponding responsivity (%/mW) at 4.18 μm under a 1 kHz chopping frequency, which is commonly used unit of responsivity for comparing bolometric detectors[26,27,34,35]. We highlight that our device achieved an *R* of 28.77%/mW (from linear fitting at $P_{in} > 0.3$ mW), equivalent to voltage responsivity of 863.19 V/W, which is sufficient for a wide range of MIR spectroscopy applications[41–43]. Details for the relationship between responsivity values in different units are described in Supplementary Note 11. This exceeds the previous state-of-the-art values for waveguide-integrated thermal-type PDs beyond 3 μm, which are 24.62%/mW at 3.8 μm in an Au antenna-assisted PD on an a-Si waveguide using the bolometric effect[27], and 1.97 V/W at 3.7 μm in a graphene-based PD on a GOS waveguide using the PTE effect[29]. A slight nonlinearity is observed at lower P_{in} ranges, potentially attributed to variations in thermo-electrical properties and changes in both G_{th} and C_{th} with temperature. We also estimated the noise-equivalent power (NEP) by taking the ratio of the noise spectral density in the off-state (see Supplementary Note 7) to responsivity at 4.18 μm, calculated as 4.03×10^{-7} W/Hz$^{0.5}$ at 1 kHz. Here, this far exceeds that of previously reported

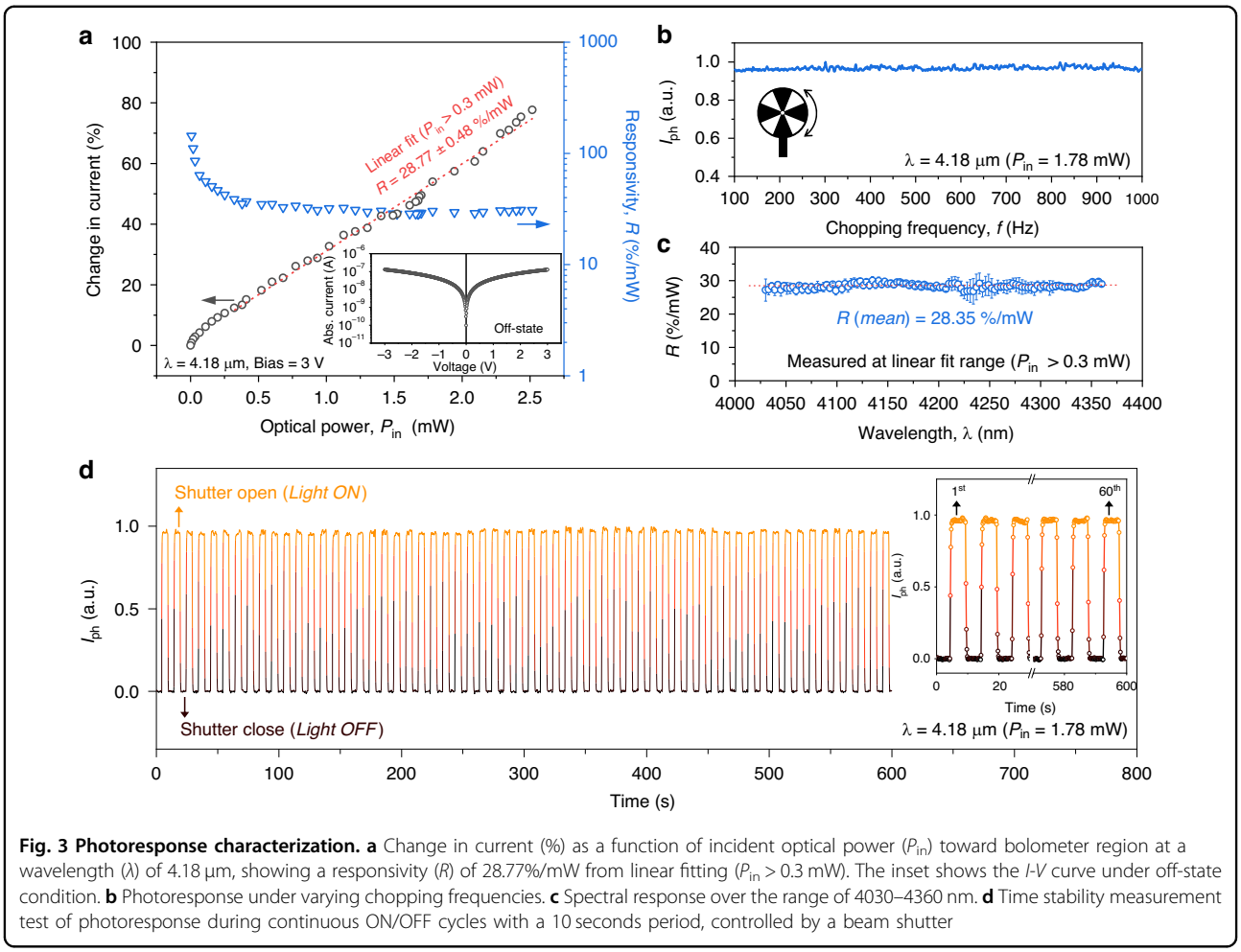

Fig. 3 Photoresponse characterization. a Change in current (%) as a function of incident optical power (P_{in}) toward bolometer region at a wavelength (λ) of 4.18 μm, showing a responsivity (R) of 28.77%/mW from linear fitting ($P_{in} > 0.3$ mW). The inset shows the *I-V* curve under off-state condition. **b** Photoresponse under varying chopping frequencies. **c** Spectral response over the range of 4030–4360 nm. **d** Time stability measurement test of photoresponse during continuous ON/OFF cycles with a 10 seconds period, controlled by a beam shutter

waveguide-integrated MIR PD using the bolometric effect (10.4 μW/Hz$^{0.5}$ at 3.8 μm)[27].

The frequency response was analyzed by varying the chopper frequency. As illustrated in Fig. 3b, our device showed stable performance with a nearly flat response up to 1 kHz (the limit of our setup). Although higher bandwidth might be beneficial, it is not a major concern in most spectroscopy applications, unlike in telecommunications and data communications, and response times of around 1 second are common for many optical gas sensors[44]. This suggests that our device is sufficiently robust for MIR lab-on-a-chip systems, which can be expected to operate at a bandwidth of several tens of kHz level, based on our previous work with the Si-on-insulator (SOI) platform in the near-infrared wavelength range[35]. We also evaluated the spectral response in the MIR band ranging from 4030 to 4360 nm. During the measurement, the P_{in} was maintained within the linear fit region ($P_{in} > 0.3$ mW). As shown in Fig. 3c, our device exhibited a broadband photoresponse with an R of around 28.35%/mW across the entire measurable range without any cutoff wavelengths. Lastly, we assessed the long-term stability with switching behavior, a key parameter for evaluating PDs. Notably, as depicted in Fig. 3d, highly stable and repeatable photocurrent generation was observed without noticeable performance degradation throughout the measurements. Here, we note that the response times were constrained by the open/close time of the beam shutter.

We have comprehensively compared our device's performance with that of previously reported MIR waveguide-integrated PDs utilizing the bolometric effect, as shown in Fig. 4. Our device exhibits a broadband responsivity of ~28.35%/mW (4030–4360 nm), the highest among its counterparts. Notably, to our knowledge, no previous reports have demonstrated waveguide-integrated bolometric PDs operating beyond the wavelength range presented in this work. Traditional Si-based photonics platforms, such as SOI with a limit of ~4 μm and suspended-Si with ~8 μm, inevitably encounter wavelength limitations due to the intrinsic material absorption of SiO_2 and Si in the MIR range[45]. Here, by leveraging the FCA-induced heating process on the Ge-OI platform that provides a broad transparency window, our approach can

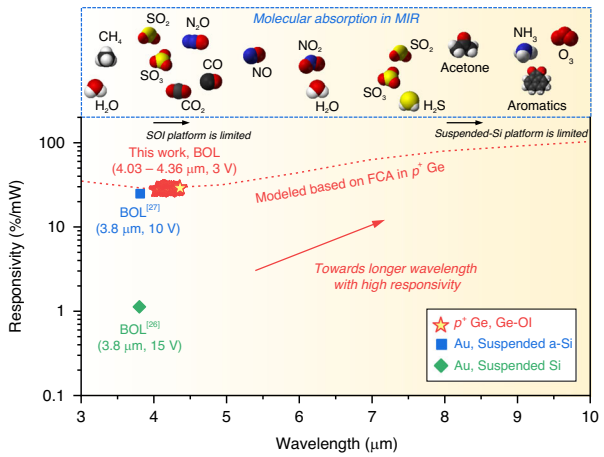

Fig. 4 Benchmark. Performance comparison of waveguide-integrated PDs using bolometric effect operating beyond 3 μm. The red dotted line represents the responsivity modeling based on FCA in p^+ Ge, aligned with our experimental results. Our approach, leveraging the FCA-induced heating mechanism and the Ge-OI platform, can cover the entire MIR spectrum for spectroscopic analysis of numerous biochemical molecules. For each reference, the mechanism of thermal detection, the absorbing medium, and the waveguide platform are indicated. BOL, bolometric. Refs. [26,27]

be widely utilized across much shorter or longer wavelength ranges in the MIR spectrum, offering significant potential for spectroscopic analysis of numerous biochemical molecules (shown in Fig. 4) without wavelength constraints. The responsivity modeling, based on FCA in Ge[32] and normalized with our experimental results, is presented in Fig. 4 (red dotted line). Moreover, our device achieves a notable improvement in NEP, over 25 times greater than previously reported waveguide-integrated PDs using the bolometric effect[26,27], without relying on noble metals or exotic materials, thus preserving full CMOS compatibility. Detailed performance characteristics, including comparisons with both bolometric and PTE detectors, are summarized in Supplementary Note 11.

Sensing demonstration

To demonstrate the label-free light–analyte interaction capabilities of our MIR PIC-based sensing platform, we arranged a 5-mm-long slot waveguide with our waveguide-integrated PD on a single Ge-OI chip, as shown in Fig. 5a. Efficient mode conversion was facilitated by strip-to-slot and slot-to-strip mode converters[36,38] positioned at the entry and exit points of the slot waveguide (detailed in Supplementary Note 10), respectively, as depicted in the optical microscope and scanning electron microscope (SEM) images in Fig. 5b. The slot waveguide, designed for high confinement within an air-clad, featured geometrical parameters of 1.8 μm width (W), 0.2 μm slot gap (G), and 500 nm height (H), as shown in the cross-sectional SEM image in Fig. 5c, highlighting the well-defined slot region where the light–analyte interaction occurs.

Here, CO_2, a major greenhouse gas contributing to global warming[46], was selected as the target analyte with a strong absorption coefficient at 4.23 μm[47]. Under the continuous-wave (CW) operation at 4.23 μm, changes in CO_2 gas concentration were detected by the photocurrent signal from our detector while simultaneously monitoring the actual CO_2 levels using a commercial gas sensor placed near the device inside the chamber. Operation conditions were maintained at 3 V and 1 kHz for biasing and chopping frequency, respectively. Figure 5d presents the normalized photocurrent signal depending on the CO_2 concentration, which exhibits a downward trend as expected from the absorption spectroscopy technique, achieving a sensitivity of 0.0696%/ppm through linear fitting. Additionally, to assess the repeatability of our optical sensing, we cycled the CO_2 valve under nitrogen (N_2) gas purging, varying the CO_2 concentration between 100 and 250 ppm. As indicated in Fig. 5e, the photocurrent signal varied clearly and repeatably with the CO_2 levels, exhibiting no memory effects. It should be noted that the response times were constrained by our experimental setup for both injecting and removing CO_2 gas within the chamber.

Discussion

In the field of integrated photonics, unlike in imaging optics, thermal detection mechanisms have yet to be fully harnessed. As noted in Supplementary Note 11, there have been limited experimental demonstrations to date (bolometric[26,27] and PTE[28,29] effect), primarily due to the challenges of implementing these mechanisms into MIR waveguide platforms. While PTE-based PDs hold promise for uncooled MIR detection with faster response times, a metric less crucial for spectroscopy applications, they face inherent limitations related to the thermoelectric materials. Low-dimensional materials, such as graphene, black phosphorus, and transition metal dichalcogenides (TMDs), are commonly used due to their high Seebeck coefficients[30], but their reliance on exotic materials and lack of CMOS compatibility restrict their widespread adoption. Additionally, the PTE effect—though not bandgap-limited—strongly depends on the material's absorption coefficient, which varies significantly with wavelength, posing challenges for broadband, wavelength-insensitive detection. Moreover, PTE detectors fundamentally rely on the temperature gradient across the material by the Seebeck effect, rather than directly on the amount of light-induced temperature change itself, implying that inconsistent thermal distribution can lead to unpredictable photoresponse. For example, the use of

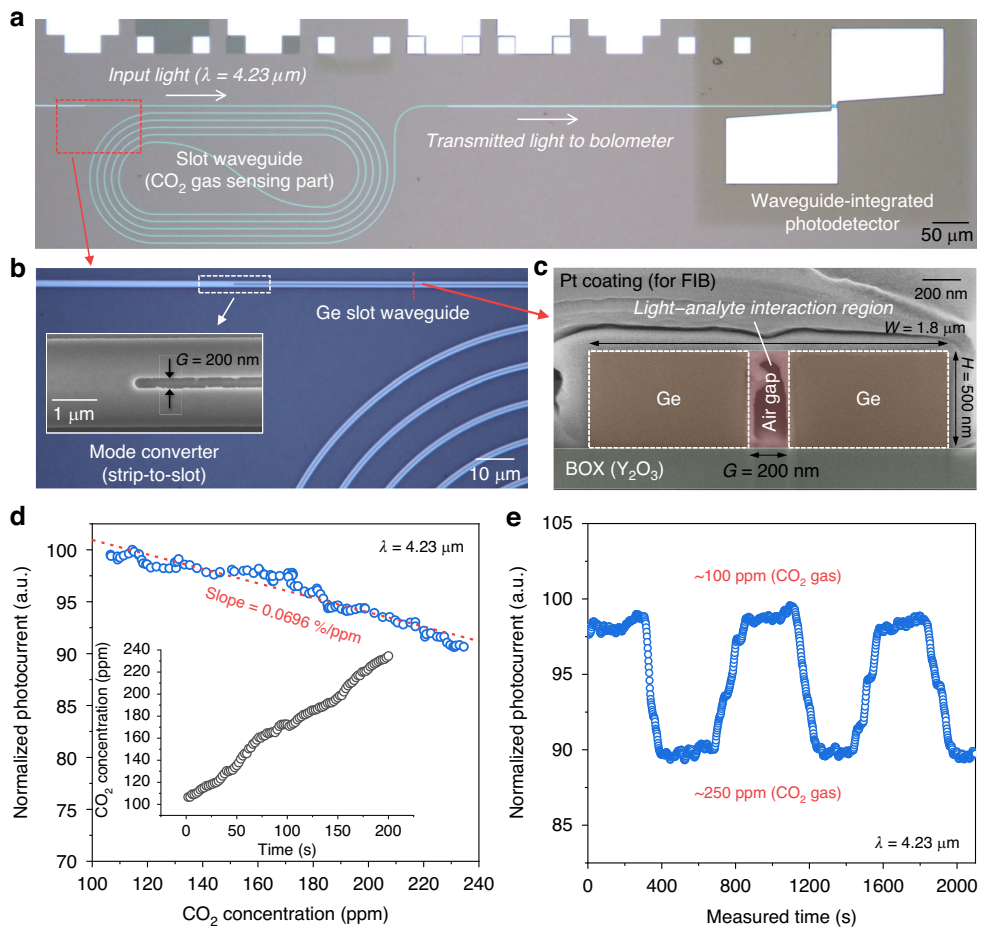

Fig. 5 Optical sensing demonstration. a Optical microscope image of the integrated photodetector connected with slot waveguide on the Ge-OI platform. **b** Magnified optical microscope image of the Ge slot waveguide. The inset shows the SEM image of the strip-to-slot mode converter. **c** Cross-sectional SEM image showing the slot waveguide with a width (*W*) of 1.8 μm and a gap (*G*) of 200 nm where the light-analyte interaction occurs. **d** Normalized photocurrent at wavelength of 4.23 μm and 3-V biasing, measured under varying CO_2 gas concentration. The inset shows the CO_2 concentration monitored by a commercial CO_2 gas sensor during the photocurrent measurement. **e** Repeatability test of photocurrent at varying CO_2 concentrations. All measurements were performed at room temperature

low-dimensional materials, particularly graphene[28,29], exacerbates this issue due to their susceptibility to fabrication tolerances, including surface unevenness and non-uniform doping, which can cause abrupt changes in the Seebeck coefficient. This uncertainty makes PTE detectors less suitable for many MIR spectroscopy applications, especially those requiring stable performance across a broad wavelength range. These challenges not only degrade photodetection capability but also impede the realization of scalable configurations with CMOS integration. Bolometric detectors, in contrast, bypass the inherent limitations of the Seebeck effect by directly converting light-induced temperature variations into changes in electrical resistance, offering a more reliable and practical solution for MIR detection without complex integration hurdles. Thus, we believe that leveraging bolometric effect presents a more attractive strategy for MIR spectroscopy, providing a clear pathway for future advancements in ultra-broadband photodetection and seamless integration with CMOS-compatible platforms.

Here, we present a straightforward, highly CMOS-compatible method for realizing bolometric photodetection within waveguide structures, serving as a blueprint for next-generation MIR PICs. The key idea of our strategy is primarily based on the FCA-induced thermalization process in heavily-doped Ge, providing a viable solution for light-to-heat conversion in MIR absorption without relying on exotic materials in CMOS or hybrid integrations. The ion implantation process is a well-established technique in current semiconductor technologies, enabling fabrication ease, cost-effectiveness, and scalability. Additionally, this approach can be readily adopted into various Si- or Ge-based MIR photonic platforms, including SOI[48], suspended-Si[45], GOS[49],

suspended-Ge[50], Ge-on-SOI[51], and Ge-OI[36–39], making it a foundry-friendly solution with the potential of process design kits (PDKs) for large-scale MIR PICs. Furthermore, as bolometry with FCA in Ge is not wavelength-specific, the operational range is extendable across the entire MIR spectrum without encountering cutoff regions.

We have achieved outstanding bolometric photoresponse characteristics through several strategic interventions: enhancing FCA-induced heating in Ge, optimizing device geometries, and improving thermoelectrical properties. Here, increasing the bias voltage may bring into reach further high photocurrent generation up to the breakdown regime at the expense of a rise in the off-state current level (detailed in Supplementary Note 8). Additionally, we can potentially push the photoresponse to a much higher level through various strategies, such as scaling down the width of bolometer region and implementing a top-contact electrode scheme above the dielectric cladding with via plugs[52], improving heat confinement within the absorbing medium. Moreover, thermal-isolation designs, such as air-trench or free-standing structures underneath the p^+ Ge region, are advantageous for boosting heating efficiency and mitigating thermal crosstalk between adjacent detectors in an array configuration, albeit at the cost of increased response time. Regarding the bolometric material of the TiO_2/Ti/TiO_2 tri-layer film stack, engineering the thickness of each layer and the annealing condition provides the flexibility to tailor electrical resistivity and thermoelectrical properties to meet the requirements of diverse spectroscopy applications[33].

We have successfully demonstrated label-free light–analyte interaction of CO_2 molecules using our PIC-based sensing system on the Ge-OI platform. While there are few reports of molecule detection utilizing MIR waveguide-based sensors with monolithic integration of detectors at room temperature[16,53], our work is pioneering in realizing molecule sensing with a CMOS-compatible solution. Moreover, given the ultra-broadband photoresponse characteristics of our approach, we envision the full potential of broad applicability in MIR spectroscopic sensing of various biochemical molecules, as well as real-time detection of multiple analytes, leveraging the label-free nature of the absorption spectroscopy method. Integrating MIR sources, such as interband cascade lasers (ICL)[54] and quantum cascade lasers (QCL)[55], could further enhance our approach, thus paving the way for a fully integrated MIR PIC-based lab-on-a-chip system. Furthermore, employing computational spectroscopy techniques, particularly through disordered structures[9,56,57], could serve as a strategy to minimize system footprint and power consumption while improving robust and agile multiplexed-detection capabilities.

Materials and methods

Simulation

The numerical simulations were conducted using the commercial simulation software packages of Ansys Lumerical, specifically the 3D-FDTD (finite-difference time-domain) and HEAT solvers. The Ge-OI structure was designed with a 500 nm-thick top layer of Ge, a 2 μm-thick Y_2O_3 BOX and a Si substrate. For simplicity in analysis, the bolometric material was modeled as a 50 nm-thick TiO_2 layer. For the steady-state thermal simulation, the heat source was imported from the absorption data obtained by the 3D-FDTD solver. The background temperature was set at 300 K. A doping concentration in the p^+ Ge region was assumed to be $10^{20}\,cm^{-3}$. Changes in refractive index and absorption coefficient were calculated based on the literature[32] and these values at specific wavelengths were approximated using linear interpolation.

Device fabrication

The fabrication process flow of the waveguide-integrated PD using the bolometric effect on the Ge-OI platform is illustrated in Supplementary Note 4. It began with the fabrication of a Ge-OI wafer, which features a 500 nm-thick top Ge, a 2 μm-thick Y_2O_3 buried oxide layer, and a Si substrate. We first prepared two types of wafers: (i) the acceptor wafer, which is a Si(100) substrate, and (ii) the donor wafer, comprising a Ge(100)/$Si_{0.5}Ge_{0.5}$/Ge strain relaxed buffer (SRB) layer stack on Si(100) substrate with a thickness of 500 nm, 10 nm, and 900 nm, respectively, grown by the metal-organic chemical vapor deposition (MOCVD) method. We introduced the $Si_{0.5}Ge_{0.5}$ and Ge SRB layers, thereby obtaining a high-quality Ge epitaxial layer with a reduction of lattice mismatch between Si and Ge. We then deposited a 1 μm-thick Y_2O_3 layer on both donor and acceptor wafers using the radio-frequency (RF) magnetron sputtering method at 150 °C, ensuring crack-free oxide films. Prior to the direct wafer bonding (DWB) process, we conducted chemical mechanical polishing (CMP) with a silica slurry to planarize the surfaces. As a result, we achieved a surface roughness of approximately 0.6 nm (root-mean-square), as measured by atomic force microscopy (AFM) analysis, which was sufficiently clean and smooth for DWB. After the surface cleaning and O_2 plasma treatment, we performed the DWB procedure, followed by the removal of the Si substrate with the sequential processes of mechanical grinding and selective etching using a diluted tetramethylammonium hydroxide (TMAH) solution at 90 °C. The Ge SRB and $Si_{0.5}Ge_{0.5}$ layers were etched away using the APM solution (ammonia hydroxide-hydrogen peroxide water mixture) and the diluted TMAH solution, respectively, resulting in the successful fabrication of the Ge-OI wafer. We then performed electron-beam (e-beam)

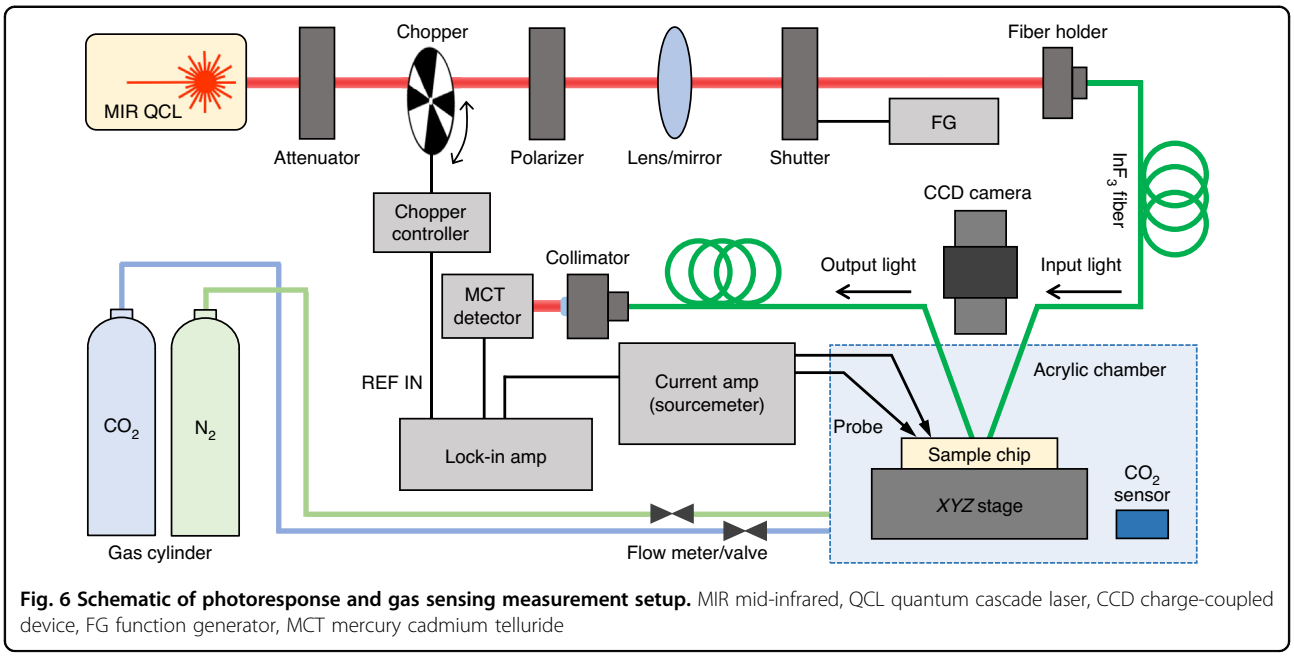

Fig. 6 Schematic of photoresponse and gas sensing measurement setup. MIR mid-infrared, QCL quantum cascade laser, CCD charge-coupled device, FG function generator, MCT mercury cadmium telluride

lithography (NanoBeam Ltd, nB5) with a negative e-beam resist (AR-N 7520) to pattern passive devices; afterwards, an inductively coupled plasma reactive ion etching (ICP-RIE) process (15 sccm C_4F_8 and 40 sccm SF_6 at a pressure of 25 mTorr, ICP power of 600 W, and RF power of 50 W) was implemented to realize an etching depth of 500 nm, followed by the removal of the e-beam resist in acetone. Prior to ion implantation for forming a p^+ Ge region, we deposited a 20 nm-thick dielectric SiO_2 layer at 150 °C by atomic layer deposition (ALD) to protect the surface of Ge layer from potential contamination or damage caused by high-energy ions and the removal of photoresist (PR) mask, used for defining the doping region (p^+ Ge) while other parts of the sample remained un-implanted. Subsequently, the ion (boron) implantation process was conducted with an implant energy of 110 keV and a dopant dose of $5 \times 10^{15}\,cm^{-2}$, followed by activation annealing at 350 °C in an N_2 ambient for 3 min. A 25 nm-thick Al_2O_3 insulating layer was grown with ALD at 170 °C to eliminate undesirable leakage currents through the Ge layer. A wet etching process using a diluted hydrofluoric acid (HF) solution was then conducted to selectively remove the SiO_2 and Al_2O_3 oxide layers, while preserving the area surrounding the p^+ Ge region. Subsequently, the bolometric material, consisting of a TiO_2/Ti/TiO_2 (25/2/25 nm) tri-layer film stack, was sequentially deposited with e-beam evaporation, followed by an acetone lift-off process. Finally, we formed an electrode stack of Ti/W (100/150 nm) with a spacing of ~2 µm through e-beam evaporation and direct current (DC) sputtering, respectively, followed by lift-off using an acetone soak.

Electrical characterization

The electrical properties of the fabricated device were characterized using a semiconductor parameter analyzer (Keithley 4200A-SCS) in a four-point probe system equipped with a thermoelectric Peltier-driven stage to precisely control of the background temperature. For DC current-voltage (*I-V*) characterization, the source measure units (SMUs) were utilized to perform a voltage sweep while simultaneously measuring the current with high resolution and accuracy. For low-frequency noise (LFN) analysis, the pulse measure units (PMUs) were employed to capture time-varying current fluctuations, followed by fast Fourier transform (FFT) calculations to analyze the data.

Photoresponse and gas sensing characterization

We built an in-house measurement system for photoresponse and gas sensing, as illustrated in Fig. 6. A tunable QCL source (Daylight Solutions MIRcat-QT-2100) under CW operation mode was modulated by a chopper (Scitec Instruments) with a specific reference frequency. Since our grating couplers (GCs) are optimized for the TE-mode[36], we employed a polarizer to maximize optical coupling efficiency. After that, the input light was launched into an indium fluoride (InF_3) single-mode optical fiber (Thorlabs) through an aspheric lens with a fiber holder. Alignment between the cleaved InF_3 fiber facet and the fabricated device was precisely achieved using a goniometer and three-axis translational stages with a charge-coupled device (CCD) camera. For the characterization of the passive components, the output light was directed into another InF_3 optical fiber and subsequently collimated into a mercury cadmium telluride (MCT) detector (VIGO

systems PVI-4TE-5). The amount of coupled optical power was calibrated using an external MCT photodiode power sensor (Thorlabs S180C). Propagation losses of strip and slot waveguides were analyzed using the cut-back method, as detailed in Supplementary Note 9. During photoresponse measurements, a programmable current amplifier (Keithley 428-PROG) with two probe contacts was used to apply bias voltage, and the resulting photoresponse signals were monitored on a lock-in amplifier (Stanford Research Systems SR830) for the signal-to-noise (SNR) ratio enhancement. For time stability measurements, a beam shutter (Thorlabs SHB1T) controlled by a function generator (FG, Tektronix AFG3022B) was implemented to turn the coupled light on and off during CW operation. All photoresponse measurements were conducted within an acrylic chamber under a pure N_2 gas purging state to mitigate any undesirable impact on CO_2 gas absorption from the atmospheric environment. For optical gas sensing demonstrations, CO_2 concentrations were regulated using a mass flow meter with a diluting pure N_2 gas into the acrylic chamber, which were precisely calibrated by a commercial CO_2 gas sensor (Sensirion AG). Here, the lowest achievable CO_2 concentration within the acrylic chamber was around 100 ppm, limited by the capabilities of our setup under an N_2 gas purging state. All measurements were carried out at room temperature.

Acknowledgements
This work is supported by the National Research Foundation of Korea (NRF) (2023R1A2C2002777, RS-2024-00407767), the KIST Institutional Program (2E33052), and the BK21 FOUR.

Author contributions
J. Shim proposed the idea, conducted the numerical simulations, and performed the measurements. J. Shim, J. Lim and I. Kim fabricated the device and built the experimental setup. J. Jeong, B. H. Kim, S. K. Kim, D.-M. Geum, and S. H. Kim contributed to the data analysis and discussion. S. H. Kim supervised the project. All authors contributed to the interpretation of results and prepared the manuscript.

Data availability
All data that support the findings of this work are available within the paper. Additional data are available from the corresponding authors upon request.

Conflict of interest
The authors declare no competing interests.

Supplementary information The online version contains supplementary material available at https://doi.org/10.1038/s41377-025-01803-3.

Received: 22 June 2024 Revised: 6 February 2025 Accepted: 26 February 2025
Published online: 19 March 2025

References

1. Kazakov, D. et al. Active mid-infrared ring resonators. *Nat. Commun.* **15**, 607 (2024).
2. Liu, M. et al. Mid-infrared cross-comb spectroscopy. *Nat. Commun.* **14**, 1044 (2023).
3. Yoo, K. M. et al. InGaAs membrane waveguide: A promising platform for monolithic integrated mid-infrared optical gas sensor. *ACS Sens.* **5**, 861–869 (2020).
4. Rodrigo, D. et al. Mid-infrared plasmonic biosensing with graphene. *Science* **349**, 165–168 (2015).
5. Wu, J. W. et al. On-chip optical gas sensors based on group-IV materials. *ACS Photonics* **7**, 2923–2940 (2020).
6. Li, K. et al. An integrated CMOS–silicon photonics transmitter with a 112 gigabaud transmission and picojoule per bit energy efficiency. *Nat. Electron.* **6**, 910–921 (2023).
7. Atabaki, A. H. et al. Integrating photonics with silicon nanoelectronics for the next generation of systems on a chip. *Nature* **556**, 349–354 (2018).
8. Sun, C. et al. Single-chip microprocessor that communicates directly using light. *Nature* **528**, 534–538 (2015).
9. Li, A. et al. Advances in cost-effective integrated spectrometers. *Light Sci. Appl.* **11**, 174 (2022).
10. Vlk, M. et al. Extraordinary evanescent field confinement waveguide sensor for mid-infrared trace gas spectroscopy. *Light Sci. Appl.* **10**, 26 (2021).
11. Yallew, H. D. et al. Sub-ppm methane detection with mid-infrared slot waveguides. *ACS Photonics* **10**, 4282–4289 (2023).
12. Ottonello-Briano, F. et al. Carbon dioxide absorption spectroscopy with a mid-infrared silicon photonic waveguide. *Opt. Lett.* **45**, 109–112 (2020).
13. Rogalski, A. Toward third generation HgCdTe infrared detectors. *J. Alloy. Compd.* **371**, 53–57 (2004).
14. Rogalski, A. & Martyniuk, P. InAs/GaInSb superlattices as a promising material system for third generation infrared detectors. *Infrared Phys. Technol.* **48**, 39–52 (2006).
15. Gordon, R. Room-temperature mid-infrared detectors. *Science* **374**, 1201–1202 (2021).
16. Ma, Y. M. et al. Heterogeneously integrated graphene/silicon/halide waveguide photodetectors toward chip-scale zero-bias long-wave infrared spectroscopic sensing. *ACS Nano* **15**, 10084–10094 (2021).
17. Huang, L. et al. Waveguide-integrated black phosphorus photodetector for mid-infrared applications. *ACS Nano* **13**, 913–921 (2019).
18. Liu, C. Y. et al. Silicon/2D-material photodetectors: from near-infrared to mid-infrared. *Light Sci. Appl.* **10**, 123 (2021).
19. Bonaccorso, F. et al. Graphene photonics and optoelectronics. *Nat. Photonics* **4**, 611–622 (2010).
20. Island, J. O. et al. Environmental instability of few-layer black phosphorus. *2D Mater.* **2**, 011002 (2015).
21. Huang, G. Y. et al. Recent progress in waveguide-integrated photodetectors based on 2D materials for infrared detection. *J. Phys. D: Appl. Phys.* **56**, 113001 (2023).
22. Talghader, J. J. et al. Spectral selectivity in infrared thermal detection. *Light Sci. Appl.* **1**, e24 (2012).
23. Stewart, J. W. et al. Nanophotonic engineering: A new paradigm for spectrally sensitive thermal photodetectors. *ACS Photonics* **8**, 71–84 (2021).
24. Jiang, W. et al. A versatile photodetector assisted by photovoltaic and bolometric effects. *Light Sci. Appl.* **9**, 160 (2020).
25. Blaikie, A. et al. A fast and sensitive room-temperature graphene nanomechanical bolometer. *Nat. Commun.* **10**, 4726 (2019).
26. Wu, Y. B. et al. Mid-infrared nanometallic antenna assisted silicon waveguide based bolometers. *ACS Photonics* **6**, 3253–3260 (2019).
27. Wu, Y. B. et al. Nanometallic antenna-assisted amorphous silicon waveguide integrated bolometer for mid-infrared. *Opt. Lett.* **46**, 677–680 (2021).
28. Goldstein, J. et al. Waveguide-integrated mid-infrared photodetection using graphene on a scalable chalcogenide glass platform. *Nat. Commun.* **13**, 3915 (2022).
29. Cai, H. J. et al. Mid-infrared waveguide-integrated and photo-thermoelectric graphene photodetector based on germanium-on-silicon platform. *APL Photonics* **9**, 096101 (2024).
30. Lu, X. W. et al. Progress of photodetectors based on the photothermoelectric effect. *Adv. Mater.* **31**, 1902044 (2019).
31. Nedeljkovic, M., Soref, R. & Mashanovich, G. Z. Predictions of free-carrier electroabsorption and electrorefraction in germanium. *IEEE Photonics J.* **7**, 2600214 (2015).
32. Zhang, L. et al. The Franz-Keldysh effect and free carrier dispersion effect in germanium. *Optik* **159**, 202–210 (2018).
33. Shim, J. et al. Tailoring bolometric properties of a TiO_x/Ti/TiO_x tri-layer film for integrated optical gas sensors. *Opt. Express* **29**, 18037–18058 (2021).

34. Shim, J. et al. TiO_x/Ti/TiO_x tri-layer film-based waveguide bolometric detector for on-chip Si photonic sensor. *IEEE Trans. Electron Devices* **69**, 2151–2158 (2022).
35. Shim, J. et al. High-sensitivity waveguide-integrated bolometer based on free-carrier absorption for Si photonic sensors. *Opt. Express* **30**, 42663–42677 (2022).
36. Lim, J. et al. Low-loss and high-confinement photonic platform based on germanium-on-insulator at mid-infrared range for optical sensing. *J. Lightwave Technol.* **41**, 2824–2833 (2023).
37. Lim, J. et al. Experimental demonstration of high-*Q* MRR based on a germanium-on-insulator platform with an yttria insulator in the mid-IR range. *Photonics Res.* **11**, A80–A87 (2023).
38. Lim, J. et al. Ultrasensitive mid-infrared optical gas sensor based on germanium-on-insulator photonic circuits with limit-of-detection at sub-ppm level. *ACS Photonics* **11**, 4268–4278 (2024).
39. Lim, J. et al. Thermally tunable microring resonators based on germanium-on-insulator for mid-infrared spectrometer. *APL Photonics* **9**, 106109 (2024).
40. Kim, I. et al. Freestanding germanium photonic crystal waveguide for a highly sensitive and compact mid-infrared on-chip gas sensor. *ACS Sens.* **9**, 5116–5126 (2024).
41. Vafaei, M. et al. Performance evaluation of a MEMS-compatible flexible graphene bolometer for chamberless NDIR gas sensing. *IEEE Sens. Lett.* **8**, 2501204 (2024).
42. Barritault, P. et al. Low power CO_2 NDIR sensing using a micro-bolometer detector and a micro-hotplate IR-source. *Sens. Actuators B: Chem.* **182**, 565–570 (2013).
43. Yadav, P. V. K. et al. Advancements of uncooled infrared microbolometer materials: A review. *Sens. Actuators A: Phys.* **342**, 113611 (2022).
44. Hodgkinson, J. & Tatam, R. P. Optical gas sensing: a review. *Meas. Sci. Technol.* **24**, 012004 (2013).
45. Penades, J. S. et al. Suspended silicon mid-infrared waveguide devices with subwavelength grating metamaterial cladding. *Opt. Express* **24**, 22908–22916 (2016).
46. Hasan, D. et al. Hybrid metamaterial absorber platform for sensing of CO_2 gas at mid-IR. *Adv. Sci.* **5**, 1700581 (2018).
47. Gordon, I. E. et al. The HITRAN2020 molecular spectroscopic database. *J. Quant. Spectrosc. Radiat. Transf.* **277**, 107949 (2022).
48. Nedeljkovic, M. et al. Mid-infrared silicon-on-insulator Fourier-transform spectrometer chip. *IEEE Photonics Technol. Lett.* **28**, 528–531 (2016).
49. Lim, J. et al. Experimental demonstration of germanium-on-silicon slot waveguides at mid-infrared wavelength. *IEEE Photonics J.* **14**, 5828709 (2022).
50. Sánchez-Postigo, A. et al. Suspended germanium waveguides with subwavelength-grating metamaterial cladding for the mid-infrared band. *Opt. Express* **29**, 16867–16878 (2021).
51. Younis, U. et al. Germanium-on-SOI waveguides for mid-infrared wavelengths. *Opt. Express* **24**, 11987–11993 (2016).
52. Lischke, S. et al. Ultra-fast germanium photodiode with 3-dB bandwidth of 265 GHz. *Nat. Photonics* **15**, 925–931 (2021).
53. Su, P. et al. Monolithic on-chip mid-IR methane gas sensor with waveguide-integrated detector. *Appl. Phys. Lett.* **114**, 051103 (2019).
54. Marschick, G. et al. Mid-infrared ring interband cascade laser: operation at the standard quantum limit. *ACS Photonics* **11**, 395–403 (2024).
55. Karnik, T. S. et al. Monolithic beam combined quantum cascade laser arrays with integrated arrayed waveguide gratings. *Opt. Express* **32**, 11681–11692 (2024).
56. Li, A. et al. On-chip spectrometers using stratified waveguide filters. *Nat. Commun.* **12**, 2704 (2021).
57. Redding, B. et al. Compact spectrometer based on a disordered photonic chip. *Nat. Photonics* **7**, 746–751 (2013).